

Research Article

Simultaneous Voltammetric Determination of Uric Acid, Xanthine, and Hypoxanthine Using CoFe_2O_4 /Reduced Graphene Oxide-Modified Electrode

Nguyen Thi Vuong Hoan ¹, Nguyen Ngoc Minh,¹ Nguyen Thi Hong Trang,¹ Le Thi Thanh Thuy ¹, Cao Van Hoang,¹ Tran Xuan Mau ², Ho Xuan Anh Vu,³ Phan Thi Kim Thu ^{3,4}, Nguyen Hai Phong ³, and Dinh Quang Khieu ³

¹Quy Nhon University, 55000, Vietnam

²Hue University, 49000, Vietnam

³University of Sciences, Hue University, 49000, Vietnam

⁴Daklak Junior College of Education, 63000, Vietnam

Correspondence should be addressed to Nguyen Thi Vuong Hoan; nguyenthivuonghoan@qnu.edu.vn, Phan Thi Kim Thu; kimthu1912@gmail.com, Nguyen Hai Phong; nhphong@hueuni.edu.vn, and Dinh Quang Khieu; dqkhieu@hueuni.edu.vn

Received 10 March 2020; Revised 5 June 2020; Accepted 22 June 2020; Published 10 July 2020

Guest Editor: Changfa Guo

Copyright © 2020 Nguyen Thi Vuong Hoan et al. This is an open access article distributed under the Creative Commons Attribution License, which permits unrestricted use, distribution, and reproduction in any medium, provided the original work is properly cited.

In the present paper, the synthesis of cobalt ferrite/reduced graphene oxide ($\text{Co}_2\text{Fe}_2\text{O}_4/\text{rGO}$) composite and its use for the simultaneous determination of uric acid (UA), xanthine (XA), and hypoxanthine (HX) is demonstrated. Cobalt ferrite hollow spheres were synthesized by using the carbonaceous polysaccharide microspheres prepared from a *D*-glucose solution as templates, followed by calcination. The $\text{CoFe}_2\text{O}_4/\text{rGO}$ composite was prepared with the ultrasound-assisted method. The obtained material was characterized by using X-ray diffraction, scanning electron microscopy, X-ray photoelectron spectroscopy, EDX elemental mapping, and nitrogen adsorption/desorption isotherms. The electrochemical behavior of UA, XA, and HX on the $\text{CoFe}_2\text{O}_4/\text{rGO}$ -modified electrode was studied with cyclic voltammetry and differential pulse voltammetry (DPV). The modified electrode exhibits excellent electrocatalytic activity towards the oxidation of the three compounds. The calibration curves for UA, XA, and HX were obtained over the range of 2.0–10.0 μM from DPV. The limits of detection for UA, XA, and HX are 0.767, 0.650, and 0.506 μM , respectively. The modified electrode was applied to the simultaneous detection of UA, XA, and HX in human urine, and the results are consistent with those obtained from the high-performance liquid chromatography technique.

1. Introduction

Uric acid (UA: 7,9-dihydro-1*H*-purine-2,6,8(3*H*)-trione), xanthine (XA: 3,7-dihydropurine-2,6-dione), and hypoxanthine (HX: 1*H*-purin-6(9*H*)-one) are oxidation products of purine nucleotide and deoxynucleotide metabolisms in human beings. The concentration of these products in human serum and urine is of great importance for clinical diagnoses, such as gout, hyperuricemia, leukemia, and pneumonia [1]. The purine oxidation products are simultaneously

determined with different techniques, such as capillary electrophoresis [2], enzymatic spectrophotometry [3], and high-performance liquid chromatography [4, 5]. However, these methods require complicated sample preparation, expensive material, and considerable time. As a result, they have limited applications. One of the alternatives to this challenge is electrochemical approaches that have attracted great interest owing to their inherent advantages, such as simplicity, high sensitivity, and low cost. The development of electrochemical analysis based on chemically modified

electrodes is a major interest in current research [6, 7]. Several electrode modifiers, such as Ru (DMSO)₄Cl₂ nanoaggregated Nafion [7], poly(bromocresol purple) [8], and poly-(L-arginine)/graphene composite [9], have been used for the simultaneous determination of UA, XA, and HX.

The synthesis and design of new electrode modifiers with numerous electrochemical sensing properties have been a great concern to many scientists. One of these modifiers is cobalt ferrite (CoFe₂O₄). Although cobalt ferrite has excellent magnetic properties, high coactivity and hardness, and moderate saturation magnetization and is used in magnetic devices, gas sensor application [10, 11], and surface-active Co(II), it has not attracted much attention in the electrochemical analysis [12]. Cobalt ferrite has a low surface area because aggregation usually occurs owing to the high surface energy of the nanoparticles, deteriorating the electrochemical activity of the material. To limit its aggregation, two approaches have usually been employed: (i) the synthesis of CoFe₂O₄ in hierarchical structures (e.g., rods, urchins, and flower-like structures) and (ii) dispersion of CoFe₂O₄ nanoparticles in carriers with a large surface area. Related to the latter, cobalt ferrite has usually been dispersed in organic or inorganic substrates. The cobalt ferrite-based materials have been employed to develop the novel electrodes for voltammetric determination of some compounds. Han et al. reported the synthesis of β -cyclodextrin-cobalt-ferrite nanocomposite to modify an electrode for catechol determination [13], Yardımcı et al. used cobalt ferrite/chitosan nanocomposite for H₂O₂ sensing [14], and Ensafi et al. determined H₂O₂ and nicotinamide adenine dinucleotide by using a cobalt ferrite/graphene oxide-modified electrode [15].

Besides graphene oxide, a derivative of this material—reduced graphene oxide (rGO)—is also an excellent substrate to disperse cobalt ferrite. The rGO with smaller oxygen content is produced from graphene oxide via chemical, thermal, or other approaches. The rGO possesses good conductivity and thermal and chemical stability [16, 17] that makes it to be used as a novel material to develop the electrodes for electrochemical sensing biomolecules [18, 19], metal ions [20], and toxic chemicals [21]. Therefore, a combination of CoFe₂O₄ with rGO is expected to result in a composite with a high surface area and electrical conductivity and a possibility of application in electrochemistry. To the best of our knowledge, the use of the CoFe₂O₄/rGO composite as an electrode modifier for the determination of UA, XA, and HA by using the voltammetry method is very limited in the literature.

In the present work, we prepared cobalt ferrite hollow spheres to fabricate a CoFe₂O₄/rGO-modified electrode. Then, we used this electrode to study the electrochemical behaviors on UA, XA, and HA oxidations by using cyclic and differential pulse voltammetry. We also addressed the analysis of real samples.

2. Experimental

2.1. Materials and Synthesis

2.1.1. Materials. All reagents are of analytical grade. Graphite (C), cobalt nitrate hexahydrate (Co(NO₃)₆·6H₂O), ferrous

sulfate heptahydrate (FeSO₄·7H₂O), uric acid (C₅H₄N₄O₃), xanthine (C₁₉H₁₆N₄O₂) and hypoxanthine (C₅H₄N₄O), and hydrochloric acid (HCl) are from Sigma-Aldrich. Acetic acid (CH₃COOH), phosphoric acid (H₃PO₄), boric acid (H₃BO₃), ammonia solution (NH₃, 25%), ethanol (C₂H₅OH), hydroperoxide (H₂O₂, 30%), and potassium hydroxide (KOH) were purchased from Daejung (Korea). The Britton–Robinson buffer solution (B–RBS) in the range of pH 2.0–10.0 was prepared from 1.0 M H₃BO₃, 1.0 M H₃PO₄, and 1.0 M CH₃COOH and was adjusted with 1 M KOH. The phosphate buffer solution (PBS) with pH 7 was prepared from 0.5 M Na₂HPO₄, 0.5 M KH₂PO₄, 0.5 M NaCl, and 0.5 M KCl. The UA, XA, and HX 2.0 × 10⁻⁵ mol · L⁻¹ standard aqueous solutions were prepared in a 0.2 mol · L⁻¹ phosphate buffer solution (pH 5) or Britton–Robinson buffer solution. Double distilled water was used to prepare all the solutions.

2.1.2. Synthesis of Cobalt Ferrite. The synthesis of CoFe₂O₄ hollow spheres was performed by adding 4 g of glucose, 1.477 g of Co(NO₃)₂·6H₂O, and 2.808 g of FeSO₄·7H₂O to 40 mL of distilled water to give a homogeneous solution. This mixture was then transferred to a Teflon-lined autoclave (100 mL) for treatment at 185°C for 8 h. The black solid was separated via centrifugation and dried in an oven at 80°C for 5 h and calcined at 500°C for 5 h. The resulting product is cobalt ferrite (Co₂Fe₂O₄).

2.1.3. Synthesis of Reduced Graphene Oxide. Graphite oxide (GrO) was prepared by using Hummers' process [22]. A mixture of 2 g of GrO and 500 mL of double distilled water was stirred under ultrasonication for 5 h to get a graphene oxide suspension (GO) (4 mg/mL GO). The GO suspension (12.5 mL GO in 250 mL distilled water) was adjusted to pH 9–10 with a 25% NH₃ aqueous solution. Then, add 0.012 g of N₂H₄·H₂O to the GO suspension and keep the mixture at 90°C for 60 min. To remove the residual N₂H₄·H₂O, the mixture was washed with a 30% H₂O₂ aqueous solution several times. The resulting mixture was neutralized until pH 7, with a 5% HCl solution. The mixture was rinsed with distilled water five times (30 mL each time). The solid, which is a graphene oxide (rGO), was collected by centrifugation and dried at 60°C for 24 h.

2.1.4. Synthesis of CoFe₂O₄/rGO. Add 10 mg of CoFe₂O₄ to 10 mL of pure ethanol and stir under the ultrasonic condition for 60 min to get a CoFe₂O₄ suspension (1 mg/mL). The rGO suspension was prepared in the same way as the CoFe₂O₄ suspension. The CoFe₂O₄/rGO suspension was obtained by mixing 10 mL of CoFe₂O₄ suspension (1 mg/mL) and 10 mL of rGO suspension (1 mg/mL) under ultrasonication for 5 h.

2.2. Apparatus. The crystal structure of the material was identified by using X-ray powder diffraction (XRD) on a Bruker D8 equipped with Cu K α radiation ($\lambda = 1.5406 \text{ \AA}$). Infrared spectra were recorded on a Fourier mid-IR InfraLUM FT-08 between 4000 and 150 cm⁻¹. Scanning electron microscopy (SEM) images were recorded on an SEM JMS-5300LV (Japan), equipped with energy-dispersive X-ray microanalysis Nova Nano SEM 450. TEM images were obtained on an FEI

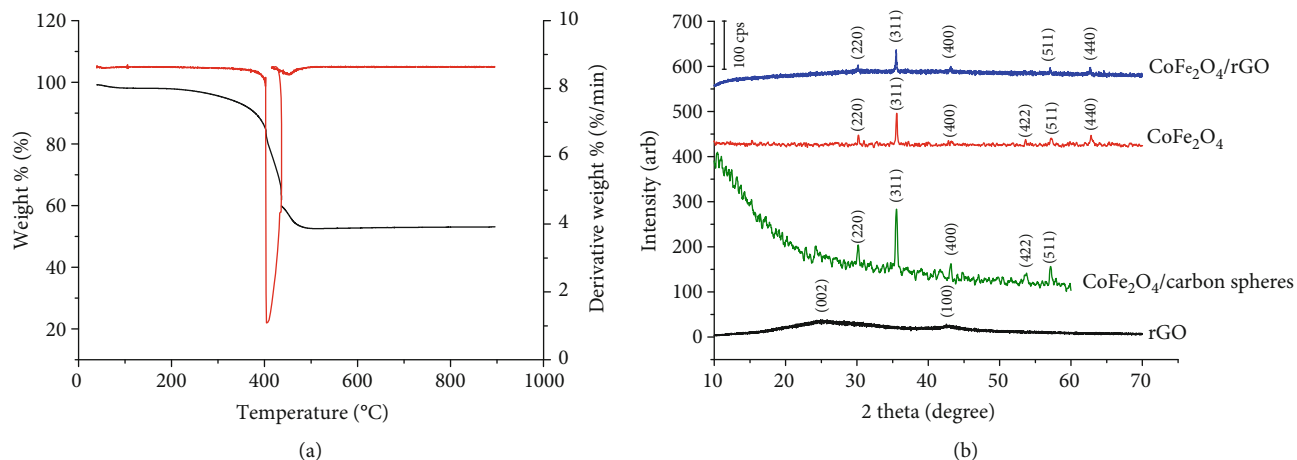


FIGURE 1: (a) TG/dTG diagram of $\text{CoFe}_2\text{O}_4/\text{carbon spheres}$. (b) XRD patterns of rGO, $\text{CoFe}_2\text{O}_4/\text{carbon spheres}$, CoFe_2O_4 , and $\text{CoFe}_2\text{O}_4/\text{rGO}$.

spirit instrument (120 kV) electron microscope. The thermal properties were measured on a Micromeritics Tristar 3000 (USA). Magnetic hysteresis loops were measured on a Vibrating Sample Magnetometer (Micro Sence Easy VSM 20130321-02) at room temperature. Energy-dispersive X-ray elemental mapping (EDX-elemental mapping) was conducted on a Horiba, Japan. Ultrasonic treatment was performed in a Cole-Parmer 8890. Electrochemistry was studied by using a CPA-HH5 in which the three-electrode system consisted of a glassy carbon electrode (GCE, a working electrode), an Ag/AgCl reference electrode (Model RE-5, BAS), and a platinum wire auxiliary electrode. The UA, XA, and HX determinations with high-performance liquid chromatography (HPLC) were performed on a Shimadzu 2030 HPLC system, with a UV-Vis detector set at 273 nm. An AC18 (6.0 mm \times 150 mm, 5 μm) chromatographic column was employed. The mobile phase is an acetonitrile/water mixture (25/75, v/v) at a flow rate of 1.5 mL \cdot min $^{-1}$, while the injection volume was 5 mL \cdot min $^{-1}$.

2.3. Analytical Procedures. The cyclic voltammetry (CV) technique was used for the preliminary studies on the electrochemical behavior of UA, XA, and HX. The differential pulse voltammetry (DPV) method was employed for the development of the electroanalytical method for the simultaneous determination of UA, XA, and HX in real samples.

Before modification, the GCE was polished with 0.05 μm alumina powder on a polishing pad, followed by sonication treatment for about two minutes in double distilled water and dried at room temperature and immediately used for modification. Two milligrams of $\text{CoFe}_2\text{O}_4/\text{rGO}$ was added to 1 mL of methanol under ultrasonic agitation for 60 min, resulting in a homogeneous black suspension. Five microlitres of $\text{CoFe}_2\text{O}_4/\text{rGO}$ suspension was dropped on the electrode surface. Then, the modified electrode was dried at ambient temperature to obtain a $\text{CoFe}_2\text{O}_4/\text{rGO}$ glassy carbon electrode.

2.4. Real Sample Analysis. Three samples of human urine, provided by a clinical laboratory, were employed to test the

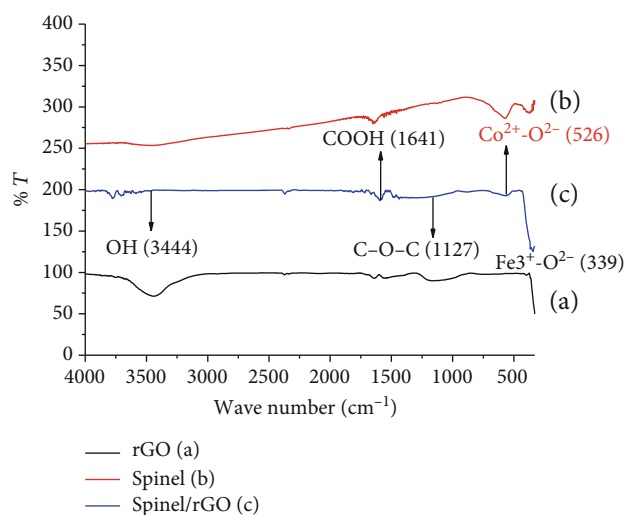


FIGURE 2: IR spectra of (a) rGO, (b) CoFe_2O_4 , and (c) $\text{CoFe}_2\text{O}_4/\text{rGO}$.

method. In detail, 1.0 mL of the urine sample was spiked with UA, XA, and HX and mixed with 2 mL of the B-RBS buffer solution to make a 10.0 mL test solution. The proposed differential pulse voltammetry method was used to detect UA, XA, and HX in the spiked solution.

3. Results and Discussion

3.1. Characterization of $\text{CoFe}_2\text{O}_4/\text{rGO}$. Figure 1(a) shows the TG/dTG curves of $\text{CoFe}_2\text{O}_4/\text{carbon hollow spheres}$ recorded in airflow from 40 to 800°C. Clearly, a weight decrease of about 2 wt.% is observed from 30 to 120°C, which is ascribed to the desorption of physically adsorbed water in the precursor. Another weight loss of about 50 wt.% at around 400°C is assigned to the combustion of rGO in the $\text{CoFe}_2\text{O}_4/\text{rGO}$ nanohybrid. This weight loss is close to the initial $\text{CoFe}_2\text{O}_4/\text{rGO}$ ratio of 1 : 1. The carbon residues are completely removed at temperatures higher than 400°C.

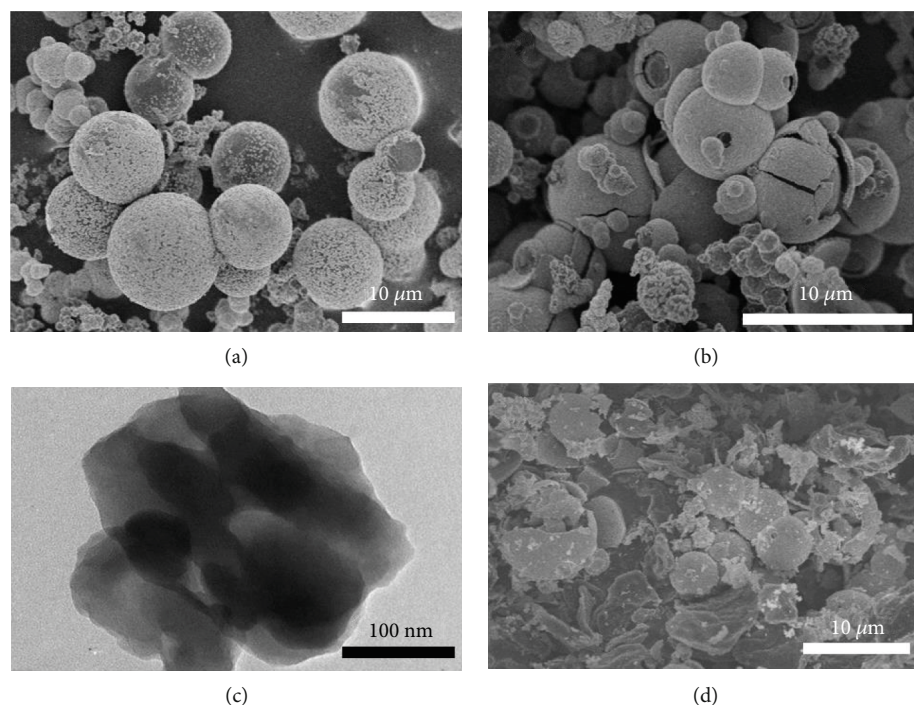


FIGURE 3: SEM images of (a) $\text{CoFe}_2\text{O}_4/\text{carbon spheres}$ and (b) CoFe_2O_4 . (c) TEM image of rGO. (d) SEM image of $\text{CoFe}_2\text{O}_4/\text{rGO}$.

The XRD pattern of rGO in Figure 1(b) presents a broad (002) diffraction peak between 20 and 35° , which corresponds to a short-range order in the stacked graphene sheets. The largely reduced interlayer spacing of about 0.342 nm (at 2θ of 26°), compared with 0.780 nm (at 2θ of 11.3°) for graphene oxide [23], indicates the formation of reduced graphene oxide, in which the oxygen functional groups are removed significantly during the reduction process. It is worth noting that the characteristic X-ray diffraction indexed as a spinel type according to JCPDS No. 00-002-1045 in $\text{CoFe}_2\text{O}_4/\text{carbon spheres}$ is observed. This means that the cobalt ferrite phase is formed during the hydrothermal treatment. Cobalt ferrite with high crystallinity is formed after the removal of the carbon template through calcination at 500°C (Figure 1(b)). The characteristic peaks of the cobalt ferrite phase in $\text{CoFe}_2\text{O}_4/\text{rGO}$ are observed in Figure 1(b). However, the large background indicates a large amorphous phase resulting from reduced graphene oxide. These results confirm the successful synthesis of the $\text{CoFe}_2\text{O}_4/\text{rGO}$ composite.

The EDX analysis shows that the molar composition of Co, Fe, O, and C in CoFe_2O_4 is 13.56, 26.81, 47.18, and 12.03%, respectively, and in $\text{CoFe}_2\text{O}_4/\text{rGO}$ is 4.81, 9.21, 34.52, and 51.46%, respectively. Correspondingly, the Co/Fe molar ratio is 1:2, which is very close to the stoichiometric ratio in the two samples. In contrast, the excessive carbon content and low Co and Fe content in $\text{CoFe}_2\text{O}_4/\text{rGO}$ indicate the presence of rGO. These results further confirm the presence of stoichiometric cobalt ferrite (CoFe_2O_4), and this is probably assigned to the high dispersion of CoFe_2O_4 on the rGO surface.

The formation of the $\text{CoFe}_2\text{O}_4/\text{rGO}$ composite was also studied by using FT-IR spectroscopy (Figure 2). On the FT-IR spectrum of rGO (Figure 2(a)), we can see vibration at

3444 cm^{-1} characteristic to OH groups and at $1641\text{--}1127\text{ cm}^{-1}$, attributed to carbonyl (C=O) and epoxy (C–O–C) groups in rGO [24]. However, these peaks have very low intensities, implying that they are removed significantly during the reduction. The typical inverse spinel ferrite structure includes two adsorption bands: one at around 339 cm^{-1} , representing the stretching vibration of the tetragonal group $\text{Fe}^{3+}\text{--O}^{2-}$, and the other at around 526 cm^{-1} , attributed to the stretching vibration of the octahedral group complex $\text{Co}^{2+}\text{--O}^{2-}$ [24] (Figure 2(b)). The characteristic vibration bands of both CoFe_2O_4 and rGO are observed in Figure 2(c), indicating successful synthesis of the $\text{CoFe}_2\text{O}_4/\text{rGO}$ composite.

The material is formed in a hollow spherical shape (Figure 3). Figure 3(a) shows the hollow spheres ($2\text{--}10\ \mu\text{m}$) with flocculent substances ($\text{CoFe}_2\text{O}_4\cdot n\text{H}_2\text{O}$) on the carbon surface. These particles remain unaltered after removing the carbon template (Figure 3(b)). The TEM image of rGO shows a stacked and crumpled morphology due to the exfoliation and restacking process [25] (Figure 3(c)). The $\text{CoFe}_2\text{O}_4/\text{rGO}$ composite consists of CoFe_2O_4 hollow spheres embroiled homogeneously with rGO sheets to form a hierarchical structure that favors the diffusion and adsorption of the analytes (Figure 3(d)).

The EDX elemental mapping in Figure 4(a) shows the SEM bright field image of the $\text{CoFe}_2\text{O}_4/\text{rGO}$ composite. The images in Figure 4 reveal that CoFe_2O_4 clusters of around 500 nm in size are embedded in the rGO matrix.

The XPS survey curve presents the existence of Co, Fe, O, and C in $\text{CoFe}_2\text{O}_4/\text{rGO}$ at 793.28 , 721.48 , 536.78 , and 288.78 eV, respectively (Figure 5(a)). The XPS spectrum Co2p possesses two main peaks at 780.67 and 796.28 eV, which are assigned to Co2p_{3/2} and Co2p_{1/2}, respectively (Figure 5(b)). The energy gap between the Co2p main peak

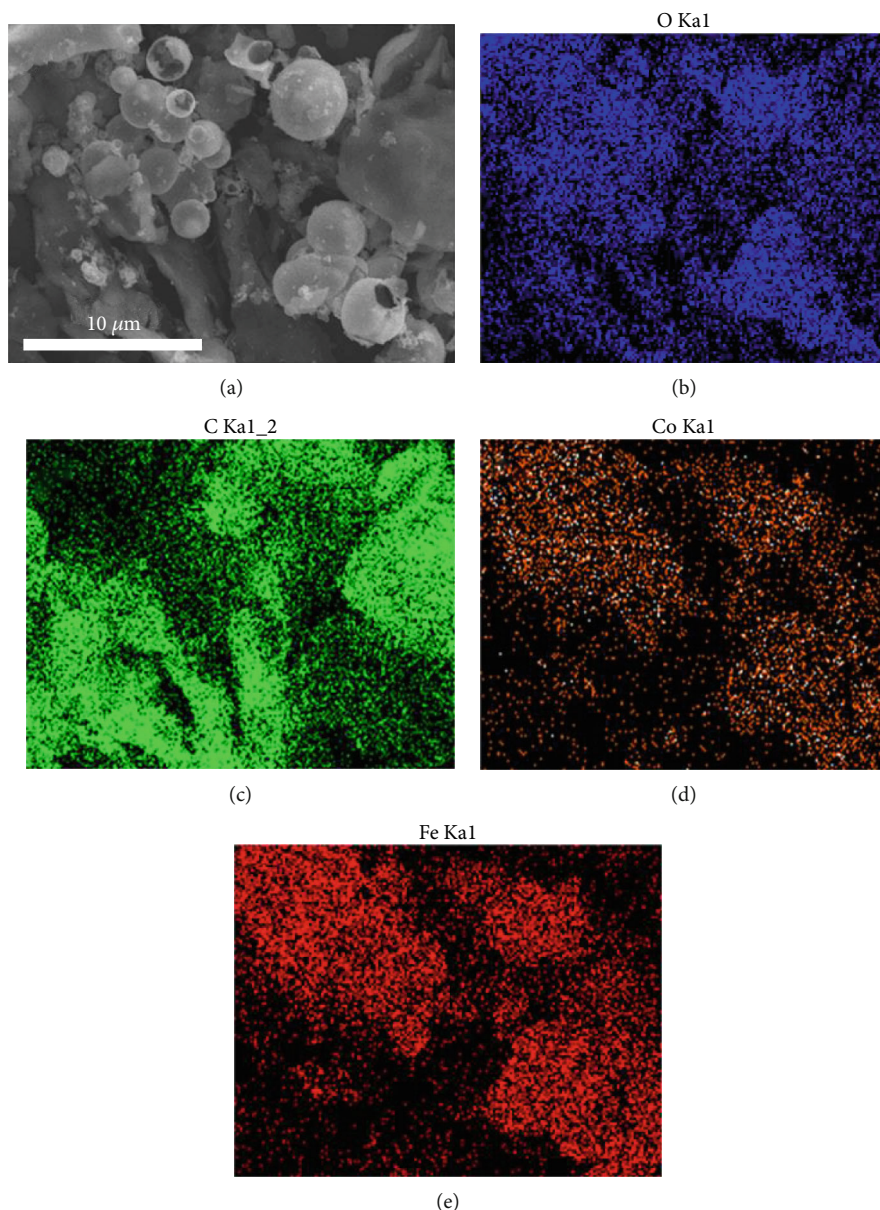


FIGURE 4: Elemental mapping of the $\text{CoFe}_2\text{O}_4/\text{rGO}$ (a) bright field image, (b) mapping of oxygen, (c) mapping of carbon, (d) mapping of cobalt, and (e) mapping of iron.

and the satellite peak can be employed to decide whether cobalt exists as Co(II) or Co(III). If the gap is *ca.* 6.0 eV, cobalt exists as Co(II), and while the gap is 9–10 eV, the cation is Co(III) [26, 27]. In our case, the energy gap of the cobalt cation is 6.62 eV for $\text{Co}2p_{1/2}$ and 5.96 eV for $\text{Co}2p_{3/2}$, and as a result, Co(II) is the main form in CoFe_2O_4 . The $\text{Fe}2p$ spectrum could be deconvoluted into two main peaks at 724.35 eV for $\text{Fe}2p_{1/2}$ and 711.13 eV for $\text{Fe}2p_{3/2}$. This spectrum has two satellite peaks with a binding energy of 733.02 and 718.83 eV (Figure 5(c)), indicating the presence of Fe(III) in the sample, which is consistent with the valence of Fe in CoFe_2O_4 [28–30]. In Figure 5(d), the $\text{O}1s$ peak is deconvoluted into two shoulder peaks at 532.56 eV and 530.46 eV, corresponding to the hydroxyl groups adsorbed on the surface and the Fe–O bond in the crystal lattice, respectively

[31]. The $\text{C}1s$ spectrum could be fitted to four carbon species at 284.58, 285.55, 286.9, and 289.46 eV, corresponding to $\text{C}/\text{C}=\text{C}$ groups in the nonoxygenated rings, C–OH, epoxy C–O–C, and carboxyl group COOH, respectively (Figure 5(e)) [32].

The magnetic hysteresis curves of the CoFe_2O_4 and $\text{CoFe}_2\text{O}_4/\text{rGO}$ composite, measured at 298 K with the field sweeping from -10000 to 10000 Oe, indicate that the two materials are ferromagnetic (Figure 6). The saturation magnetization is $60.2 \text{ emu}\cdot\text{g}^{-1}$ for CoFe_2O_4 and $48.6 \text{ emu}\cdot\text{g}^{-1}$ for $\text{CoFe}_2\text{O}_4/\text{rGO}$. These values are slightly higher than those of other cobalt-ferrite-based materials, reported previously [32–34].

The specific surface area and pore volume of the materials were determined by using the nitrogen sorption

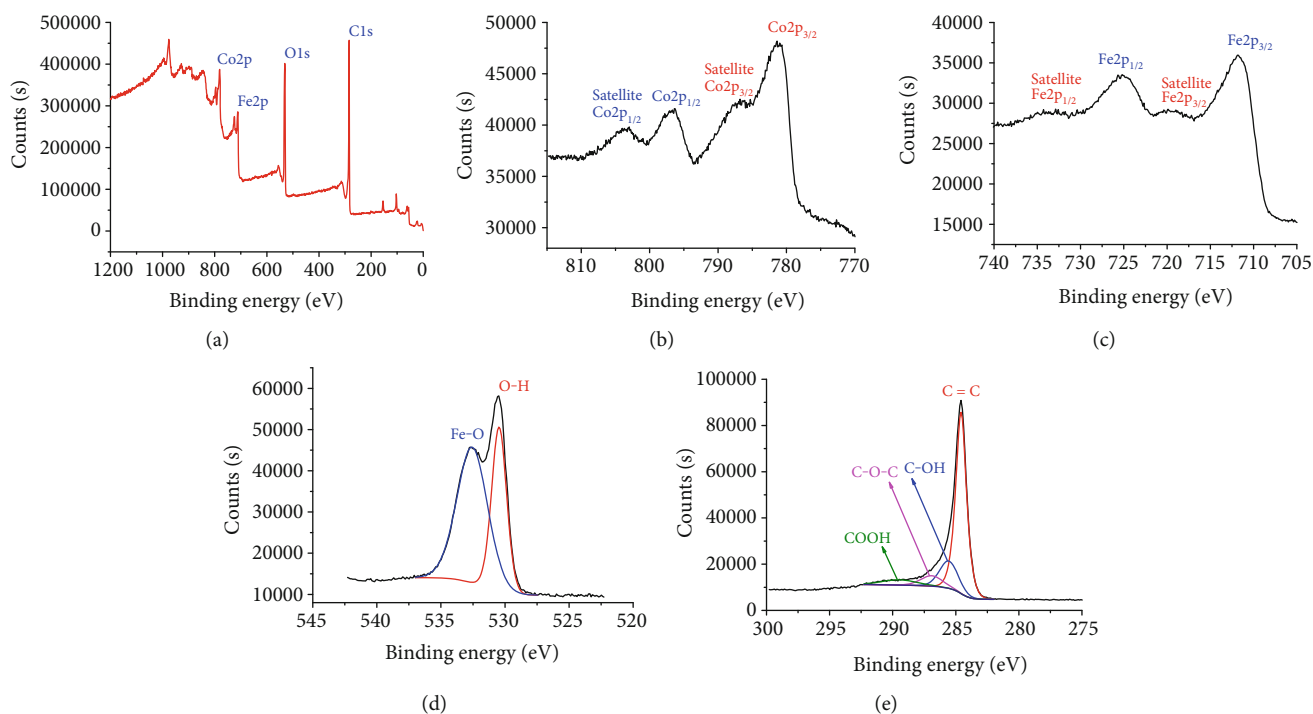


FIGURE 5: XPS spectrum of $\text{CoFe}_2\text{O}_4/\text{rGO}$: (a) survey spectrum; (b) XPS spectrum $\text{Co}2p$; (c) XPS spectrum $\text{Fe}2p$; (d) XPS spectrum $\text{O}1s$; (e) XPS spectrum $\text{C}1s$.

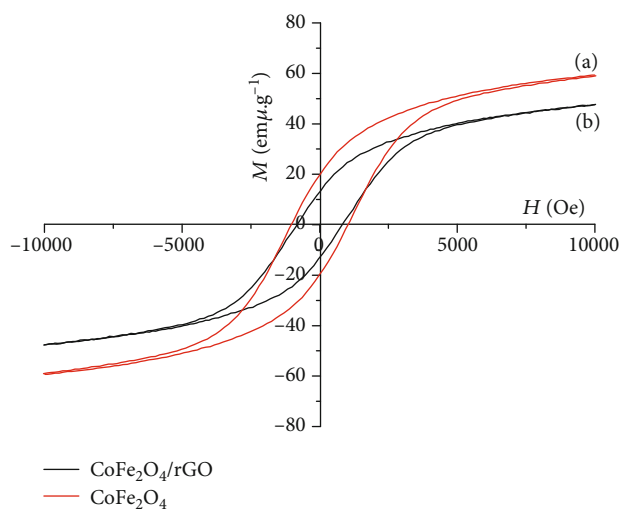


FIGURE 6: Magnetic saturation curves of (a) CoFe_2O_4 and (b) $\text{CoFe}_2\text{O}_4/\text{rGO}$.

technique, with a typical isotherm shown in Figure 7. The isotherms of rGO, CoFe_2O_4 , and $\text{CoFe}_2\text{O}_4/\text{rGO}$ exhibit type IV with hysteresis loops at high relative pressures. This indicates the presence of interparticle and nonordered mesoporosity in the materials. The BET surface area is $319 \text{ m}^2 \cdot \text{g}^{-1}$ for rGO, $16 \text{ m}^2 \cdot \text{g}^{-1}$ for CoFe_2O_4 , and $77 \text{ m}^2 \cdot \text{g}^{-1}$ for $\text{CoFe}_2\text{O}_4/\text{rGO}$. The surface area of the $\text{CoFe}_2\text{O}_4/\text{rGO}$ composite is nearly fivefold compared with that of pure CoFe_2O_4 . These findings indicate that cobalt ferrite particles are highly dispersed on the rGO matrix, and the material possesses a large surface area.

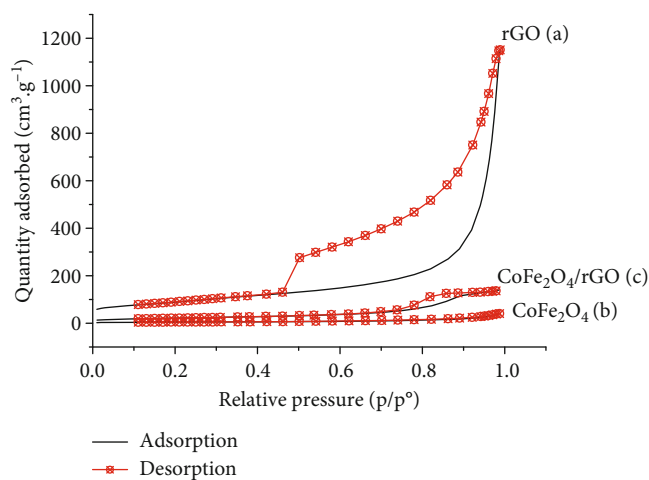


FIGURE 7: Nitrogen adsorption/desorption of (a) rGO, (b) CoFe_2O_4 , and (c) $\text{CoFe}_2\text{O}_4/\text{rGO}$.

3.2. Electrochemical Performance of $\text{CoFe}_2\text{O}_4/\text{rGO}$ -Modified Electrode

3.2.1. Voltammetric Behavior of Different Electrodes. As seen in Figure 8, all electrodes provide an anodic peak current (I_a) for the analytes, and the highest peak current with low standard deviation is observed on CoFe_2O_4 -rGO/GCE for all the analytes.

The CoFe_2O_4 -rGO/GCE is favorable for electron transfer and oxidation. Therefore, this modified electrode was selected for further experiments.

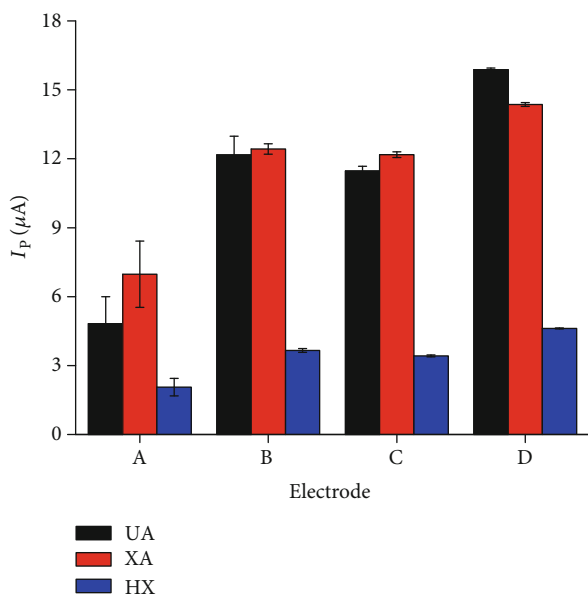


FIGURE 8: Anodic peak current (I_p) of UA, XA, and HX at bare GCE (A), $\text{CoFe}_2\text{O}_4/\text{GCE}$ (B), rGO/GCE (C), and $\text{CoFe}_2\text{O}_4\text{-rGO}/\text{GCE}$ (D). Conditions: $E_{\text{acc}} = -0.3 \text{ V}$, $t_{\text{acc}} = 20 \text{ s}$, $\Delta E = 120 \text{ mV}$, and $\nu = 20 \text{ mV} \cdot \text{s}^{-1}$ ($C_{\text{UA}} = C_{\text{XA}} = C_{\text{HX}} = 2 \times 10^{-5} \text{ M}$; 0.2 M PBS pH 7, $n = 4$).

3.2.2. Effect of Amount of Electrode Modifier. The amount of $\text{CoFe}_2\text{O}_4/\text{rGO}$ on the electrode surface is related to the thickness of the cast film and responsible for the total specific surface area. Therefore, this amount affects the adsorption of UA, XA, and HX on the electrode surface and, thus, the anodic peak current of UA, XA, and HX. To study this effect, we changed the volume of the $\text{CoFe}_2\text{O}_4/\text{rGO}$ suspension ($1.0 \text{ mg} \cdot \text{mL}^{-1}$) during the measurements. At the beginning of the volume range, the I_a increases with the volume of the $\text{CoFe}_2\text{O}_4/\text{rGO}$ suspension, owing to the increasing amount of UA, XA, and HX adsorbed on the modified electrode surface. Later, the I_a changes slightly when the volume of the $\text{CoFe}_2\text{O}_4/\text{rGO}$ suspension exceeds $5 \mu\text{L}$, indicating an insignificant influence of the film thickness on the adsorption of the analytes (Figure 9). This also suggests a rapid electron transfer within the $\text{CoFe}_2\text{O}_4/\text{rGO}$ film. However, when the volume of the $\text{CoFe}_2\text{O}_4/\text{rGO}$ suspension is greater than $7.5 \mu\text{L}$, the I_a tends to decrease due to larger film thickness and the increasing mass transfer resistance against the electron transfer. In this work, the amount of $\text{CoFe}_2\text{O}_4/\text{rGO}$ suspension on the GCE surface was selected at $5 \mu\text{L}$.

3.2.3. Effects of pH. The pH of the solution has a remarkable influence on the UA, XA, and HX electrooxidation on the $\text{CoFe}_2\text{O}_4/\text{rGO}$ -GCE. Figure 10(a) illustrates the DPV curves of UA, XA, and HX on the modified electrode in the pH range of 2–10. As shown in Figure 10(b), when the pH of the solution is lower than 4, the I_a of all analytes decreases with pH. At a pH higher than 6, only the I_a of XA increases with pH and reaches a maximum at pH 6. However, the I_a of UA and HX tends to reduce until pH reaches 7. Afterward, they change irregularly as pH increases. The dependence of the peak current of UA, XA, and HX on pH is complicated, but a decreasing tendency is observed with all the analytes

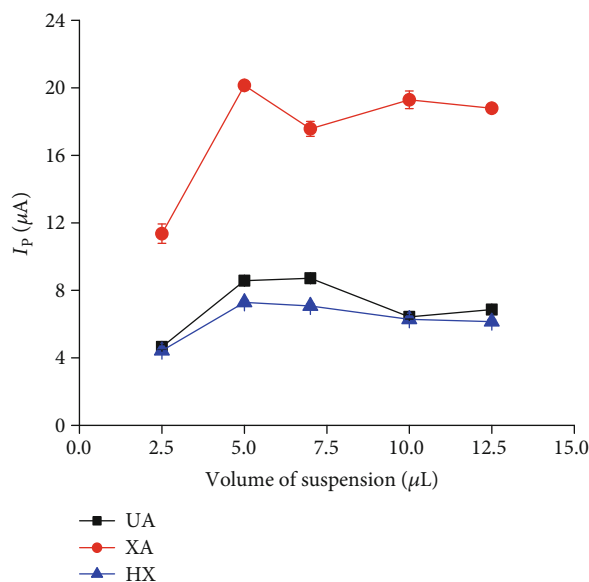


FIGURE 9: Effects of the amount of $\text{CoFe}_2\text{O}_4/\text{rGO}$ on the GCE on the anodic peak currents (I_p) of $C_{\text{UA}} = C_{\text{XA}} = C_{\text{HX}} = 2 \times 10^{-5} \text{ M}$ in 0.2 M B-RBS pH 7. Other conditions are as in Figure 8.

(Figure 10(b)). This may result from the adsorption behavior of UA, XA, and HX on the $\text{CoFe}_2\text{O}_4/\text{rGO}$ -GCE. UA, XA, and HX are known as protic aromatic molecules and can become deprotonated to form negatively charged species (anions) at higher pH. Simultaneously, the surface of $\text{CoFe}_2\text{O}_4/\text{rGO}$ -GCE also becomes negatively charged at high pH. As a result, less intensive adsorption of the analytes on the electrode might take place, thus reducing the I_a .

The pH effects on peak potentials (E_p) for UA, XA, and HX oxidations on the $\text{CoFe}_2\text{O}_4/\text{rGO}$ -GCE were also studied. The E_p values shift to more negative potential with pH, and the plots of E_p vs. pH exhibit high linearity with high determination coefficients (>0.99) (Figure 10(c)). The regression equations are expressed as follows:

$$\text{UA} : E_{p,\text{UA}} = (0.607 \pm 0.010) + (-0.061 \pm 0.001) \times \text{pH},$$

$$r = 0.9978.$$

$$\text{XA} : E_{p,\text{XA}} = (0.976 \pm 0.010) + (-0.056 \pm 0.001) \times \text{pH},$$

$$r = 0.9976.$$

$$\text{HX} : E_{p,\text{HX}} = (1.346 \pm 0.012) + (-0.060 \pm 0.002) \times \text{pH},$$

$$r = 0.9970.$$

(1)

The slopes of the lines are -0.061 , -0.056 , and -0.060 for UA, XA, and HX, respectively, and they are close to the theoretical slope of -0.0599 V/pH . This indicates that the oxidation of UA, XA, and HX involves an equal number of electrons and protons.

3.2.4. Effects of Scan Rate. The effect of the scan rate on electrochemical signals of UA, XA, and HX was also assessed by

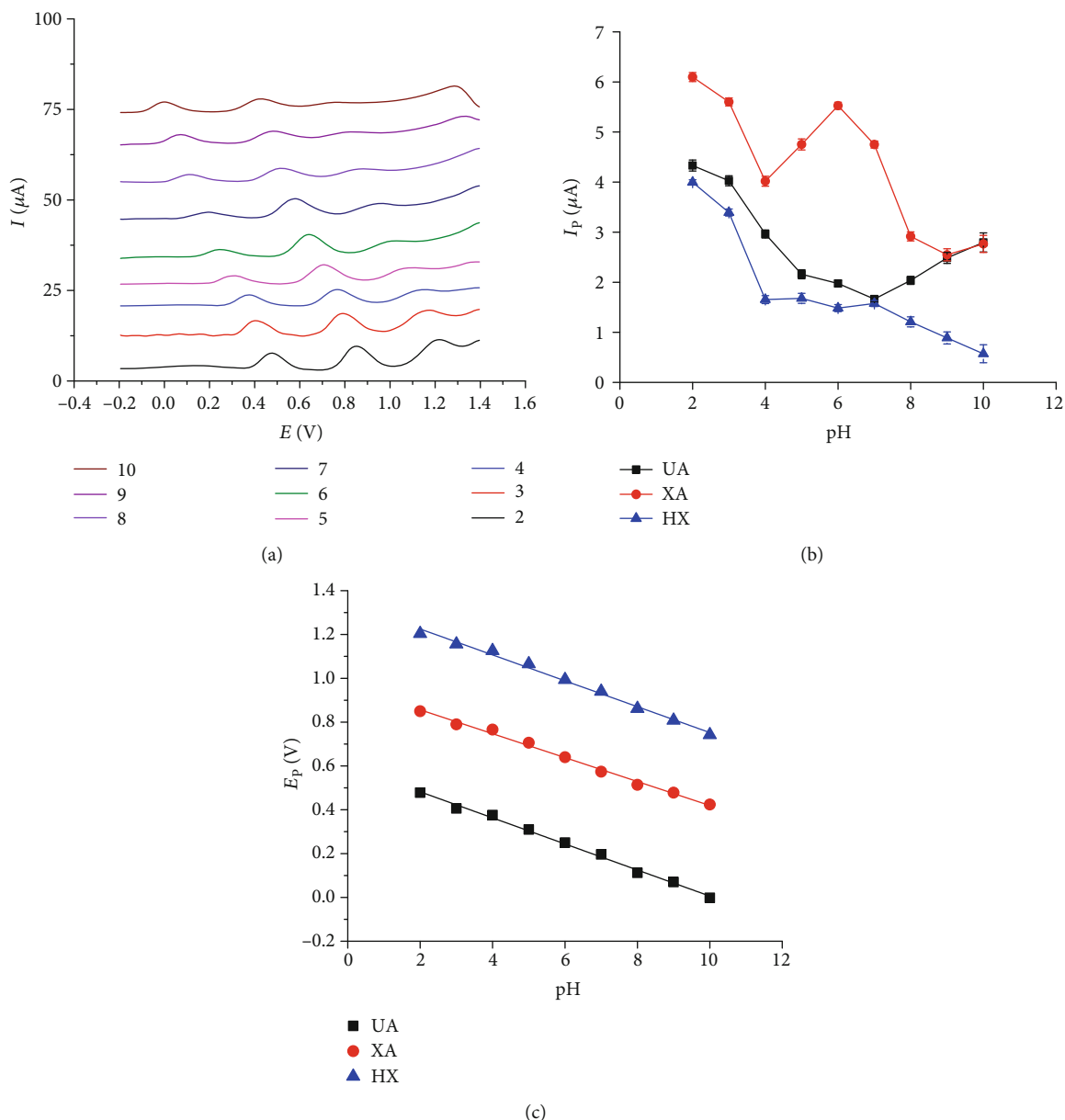


FIGURE 10: (a) DPV curves of UA, XA, and HX oxidations on the modified electrode at different pH. (b) Effects of pH on the anodic peak currents (I_p). (c) The linear plot of anodic peak current (I_p) vs. pH ($C_{\text{UA}} = C_{\text{XA}} = C_{\text{HX}} = 2 \times 10^{-5}$ M in 0.2 M B-RBS). Other conditions are as in Figure 8.

changing the scan rate from 50 to 500 $\text{mV}\cdot\text{s}^{-1}$ (Figure 11). Figure 11(a) presents the scan rate effect of electrochemical responses studied with the CV method. The linear plot of the peak current vs. the square root of the scan rate was conducted to estimate whether the electrooxidation reaction is controlled by diffusion or adsorption. If the plot of I_p vs. $\nu^{1/2}$ passes the origin, this process is controlled by diffusion; otherwise, it is controlled by adsorption [35, 36]. The plots of $I_{p,\text{UA}}$, $I_{p,\text{XA}}$, and $I_{p,\text{HX}}$ vs. $\nu^{1/2}$ are highly linear ($r = 0.9588 \div 0.9866$, $p < 0.001$) (Figure 11(b)). The number in the parentheses presents the 95% confidence interval. No lines pass the origin because all the intercepts are greater than zero (varying from 0.690 to 6.770 for UA, 10.913 to 16.767 for XA, and 1.799 to

7.843 for HX at 95% confidence—Equations (2), (3), and (4)). This indicates that the electrode process is controlled by adsorption.

$$I_{p,\text{UA}} = (3.730 \pm 3.040) + (1.276 \pm 0.189) \times \nu^{1/2},$$

$$r = 0.9588, \quad (2)$$

$$I_{p,\text{XA}} = (13.840 \pm 2.927) + (2.182 \pm 0.182) \times \nu^{1/2},$$

$$r = 0.9863, \quad (3)$$

$$I_{p,\text{HX}} = (4.771 \pm 3.072) + (1.435 \pm 0.191) \times \nu^{1/2},$$

$$r = 0.9663. \quad (4)$$

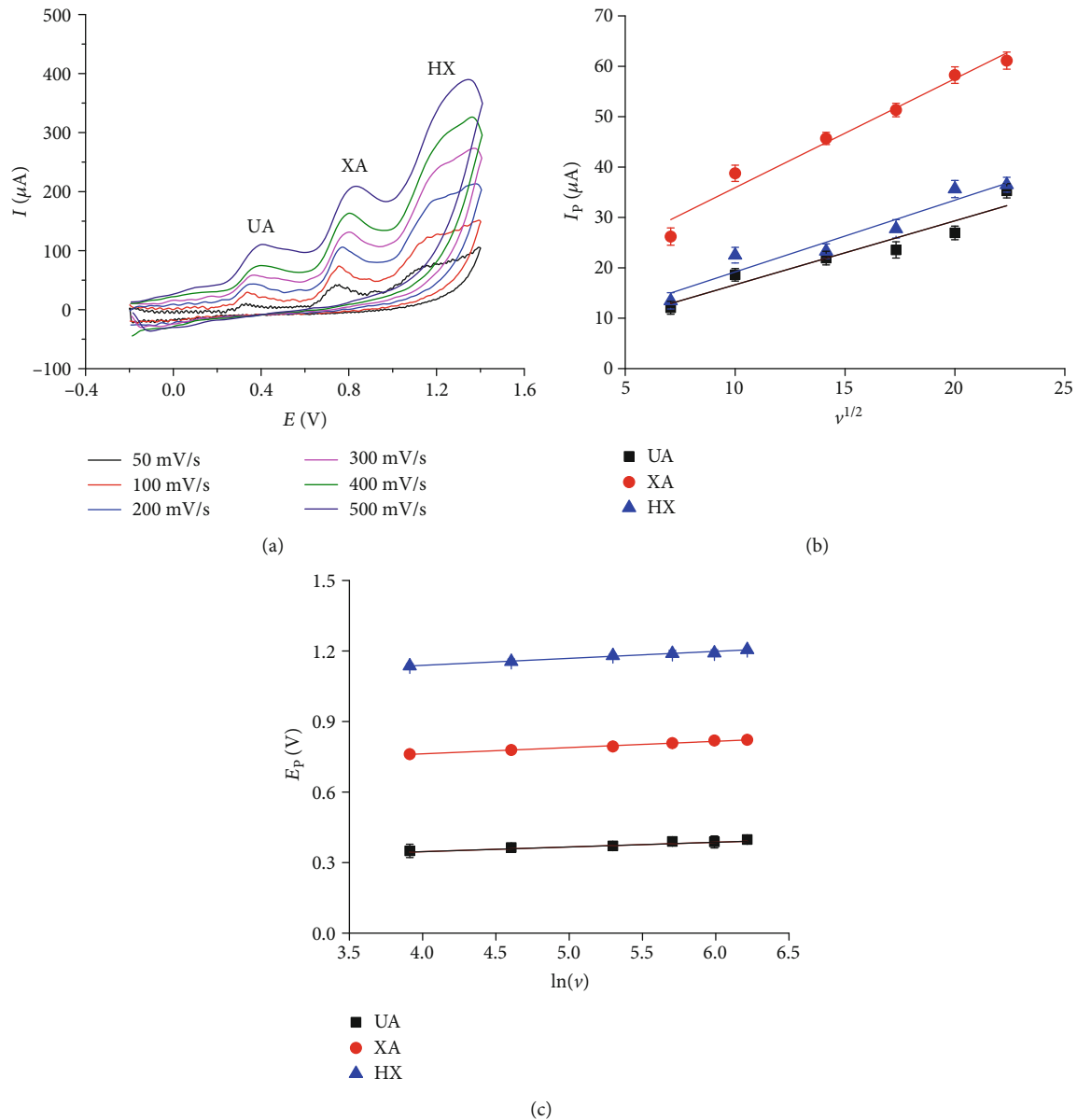


FIGURE 11: (a) DPV curves of UA, XA, and HX oxidations at the $\text{CoFe}_2\text{O}_4/\text{rGO-GCE}$. (b) The plot of anodic peak current (I_a) vs. $v^{1/2}$. (c) The plot of anodic peak potential (E_a) vs. $\ln(v)$. Conditions: $E_{\text{acc}} = -0.3$ V, $t_{\text{acc}} = 20$ s, $E_{\text{range}} = -0.0 \div +1.4$ V ($C_{\text{UA}} = C_{\text{XA}} = 5 \times 10^{-4}$ M and $C_{\text{HX}} = 10^{-3}$ M in 0.2 M B-RBS pH 5).

The relationship of the anodic potential vs. the natural logarithm of the scan rate is expressed by the Laviron equation [37].

$$E_p = E^\circ - \frac{R \times T}{(1 - \alpha) \times n \times F} \ln \frac{R \times T \times K_s}{(1 - \alpha) \times n \times F} + \frac{R \times T}{(1 - \alpha) \times n \times F} \times \ln(v), \quad (5)$$

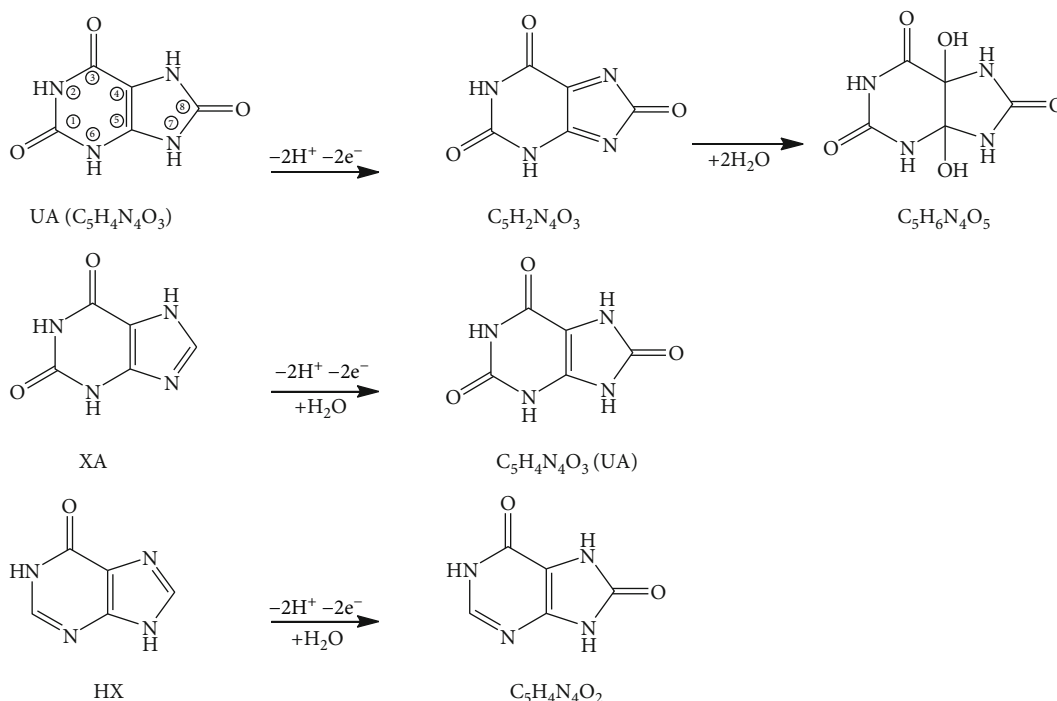
where K_s is the electron rate constant of the surface-confined redox couple, n is the number of electrons transferred, α is the charge transfer coefficient, v is the scan rate ($\text{V} \cdot \text{s}^{-1}$), E° is the formal redox potential, $T = 298$ K, $R = 8.314 \text{ J} \cdot \text{mol}^{-1} \cdot \text{K}^{-1}$, and $F = 96480 \text{ C} \cdot \text{mol}^{-1}$.

The plots of the anodic peak potential vs. the natural logarithm of the scan rate are presented in Figure 11(c). The regression equation is expressed in Equations (6)–(8).

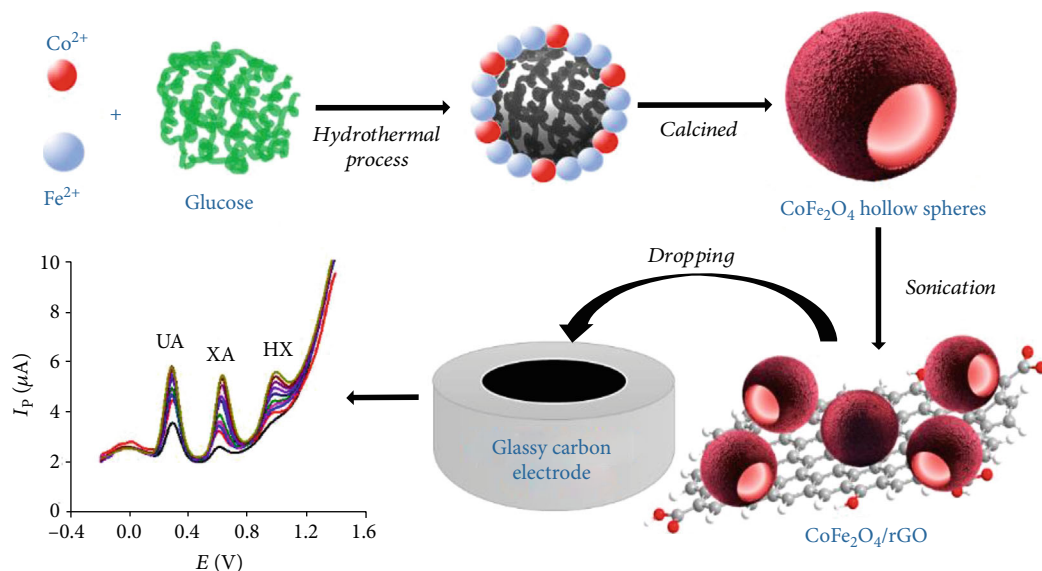
$$E_{p,\text{UA}} = (0.270 \pm 0.012) + (0.021 \pm 0.002) \times \ln(v), \quad r = 0.977 \quad (6)$$

$$E_{p,\text{XA}} = (0.654 \pm 0.006) + (0.027 \pm 0.001) \times \ln(v), \quad r = 0.996, \quad (7)$$

$$E_{p,\text{HX}} = (0.994 \pm 0.019) + (0.030 \pm 0.004) \times \ln(v), \quad r = 0.978. \quad (8)$$



SCHEME 1: Proposed mechanism for the oxidation of UA, XA, and HX.



SCHEME 2: Proposed mechanism for the electrode process of UA, XA, and HX oxidations.

The values of $n \times \alpha$ for UA, XA, and HX are 1.222, 0.950, and 0.856, respectively. For the irreversible system, α is assumed to be 0.5 [38]. Therefore, the average values of n are 2.444, 1.900, and 1.912. Because the number of electrons transferred is an integer, this number should be 2 in this case for all analytes. Therefore, the oxidation of UA, XA, and HX involves two electrons and two protons. This is consistent with previous work [8]. The mechanism for the oxidation of the analytes is proposed in Scheme 1.

The CoFe₂O₄/rGO film possesses a large number of negatively charged surface functional groups (–OH) and

electron-rich oxygen atoms (epoxide, OH, C=O), and they could interact with the purine derivatives (in this case, they are UA, XA, and HX). Furthermore, the CoFe₂O₄/rGO-modified electrode exhibits a larger real surface, π - π conjugated bonds, an abundant number of active sites, and better electronic conductivity, which leads to a strong interaction between the purine derivatives and the electrode interface. Therefore, the electrochemical oxidation of UA, XA, and HX may be substantially accelerated in the presence of the CoFe₂O₄/rGO film. This might result from the enhanced rate of electron transfer and electrocatalytic activity towards

TABLE 1: Tolerance limit of interfering species at $C_{UA} = C_{XN} = C_{HX} = 10^{-5}$ M in 0.2 M PBS pH 5.

Interferent	Interferent/analyte molar ratio	UA		XA		HX	
		I_p (μ A)	RE (%)	I_p (μ A)	RE (%)	I_p (μ A)	RE (%)
Paracetamol	10 : 1	4.25	17.49	3.68	-5.00	1.96	-1.23
Ascorbic acid	50 : 1	4.81	28.05	3.75	-7.57	2.03	-4.86
D-Glucose	1000 : 1	3.40	-1.92	3.65	0.06	1.96	-1.11
KCl	20 : 1	1.429	2.15	4.574	1.64	2.60	0.902
Na ₂ CO ₃	20 : 1	0.562	-5.23	3.66	2.52	2.262	4.31
MgSO ₄	100 : 1	0.620	-1.27	3.530	-3.29	2.085	-5.51

TABLE 2: Mean values of I_p , RSD, and RSD_H.

	C (M)	$I_{p,average}$ (μ A)	SD	RSD (%)	$1/2 \times RSD_H$ (%)
EPX 1	$C_{UA} = 10^{-5}$	1.968	0.04	2.17	5.66
	$C_{XA} = 10^{-5}$	0.918	0.02	2.04	5.66
	$C_{HX} = 10^{-5}$	0.381	0.01	2.33	5.66
EPX 2	$C_{UA} = 5 \times 10^{-5}$	3.299	0.05	1.49	4.44
	$C_{XA} = 5 \times 10^{-5}$	2.788	0.03	1.18	4.44
	$C_{HX} = 5 \times 10^{-5}$	1.338	0.01	1.05	4.44
EPX 3	$C_{UA} = 10^{-4}$	2.604	0.06	2.29	4.00
	$C_{XA} = 10^{-4}$	3.423	0.04	1.11	4.00
	$C_{HX} = 10^{-4}$	1.718	0.03	1.50	4.00

SD: standard deviation; RSD: relative standard deviation. B-RBS pH = 5; $n = 4$.

the oxidation of UA, XA, and HX. The argument is illustrated in Scheme 2.

3.2.5. Interferent Study. For evaluating the selectivity of the modified electrode, several possible interferents were evaluated for their behavior in the determination of UA, XA, and HX (equal concentration of 2.0×10^{-5} mol \cdot L⁻¹). The tolerance limit is the maximum concentration of a foreign substance that causes an approximately $\pm 5\%$ relative error in the determination. It is found that 10-fold of paracetamol and 50-fold of ascorbic acid do not interfere with the peak current of XA and HX but significantly affect that of UA. However, 1000-fold of D-glucose, 20-fold of KCl and Na₂CO₃, and 100-fold of MgSO₄ do not interfere with the determination of UA, XA, and HX (Table 1). These findings indicate that the present method can be used for real samples.

3.2.6. Repeatability, Linear Range, and Limit of Detection. The repeatability of I_p at the CoFe₂O₄/rGO-GCE was estimated by comparing the relative standard deviation (RSD) with the relative standard deviation calculated from Horwitz's equation: $RSD_H = 2^{1-0.5 \times \lg C}$, where C is the concentration in mole fraction. If the RSD is less than $1/2 \times RSD_H$, the repeatability is acceptable [39]. Each signal of I_p was obtained by conducting a series of four successive measurements at three concentrations. Table 2 displays the values of RSD and the $1/2 \times RSD_H$ predicted, and we can see that all the measurements are repeatable. Therefore, the CoFe₂O₄/rGO-

GCE can be used repeatedly for the detection of UA, XA, and HX at low or high concentrations.

Under optimum conditions, the peak current in stripping voltammetry exhibits two linear ranges: 2μ M to 10μ M (P1) and 10μ M to 35μ M (P2) (Figure 12). The linear regression equations are as follows:

$$UA : I_{p1,UA} = (1.301 \pm 0.039) + (0.145 \pm 0.006) \times C_{UA},$$

$$r = 0.9976,$$

$$I_{p2,UA} = (2.387 \pm 0.055) + (0.038 \pm 0.002) \times C_{UA},$$

$$r = 0.9928.$$

$$XA::I_{p1,XA} = (0.277 \pm 0.029) + (0.126 \pm 0.004) \times C_{XA},$$

$$r = 0.9982,$$

$$I_{p2,XA} = (1.017 \pm 0.074) + (0.059 \pm 0.003) \times C_{XA},$$

$$r = 0.9945.$$

$$HX::I_{p1,HX} = (0.119 \pm 0.008) + (0.044 \pm 0.001) \times C_{HX},$$

$$r = 0.9989,$$

$$I_{p2,HX} = (0.270 \pm 0.025) + (0.031 \pm 0.0001) \times C_{HX},$$

$$r = 0.9976.$$

(9)

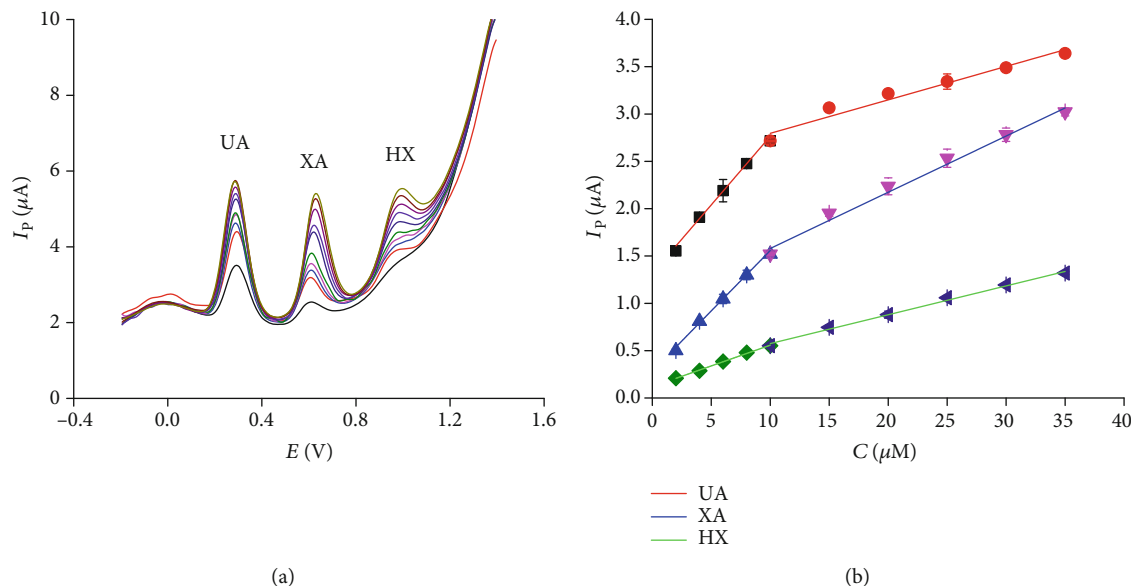


FIGURE 12: (a) DPV curves for UA, XA, and HX with different concentrations in B-RBS 0.2 M pH 5. (b) The plot of I_a vs. concentration. Other conditions are as in Figure 8.

TABLE 3: Comparison of the proposed method with other electrochemical approaches for the simultaneous determination of UA, XA, and HX.

Electrode modifier	Analytes	Linear range (μM)	LOD (μM)	References
Ru (DMSO) ₄ Cl ₂ nanoaggregated Nafion	UA	100–700	0.372	[7]
	XA	50–500	2.35	
	HX	50–300	2.37	
Preanodized nontronite	UA	2.0–40	0.42	[6]
	XA	2.0–40	0.07	
	HX	4.0–30	0.34	
Poly(bromocresol purple)	UA	0.5–120	0.20	[8]
	XA	0.1–100	0.06	
	HX	20–80	0.12	
Poly-(L-arginine)/graphene composite	UA	0.1–10	0.05	[41]
	XA	0.1–10	0.05	
	HX	0.2–20	0.1	
Pyrolytic graphite	UA	10–500	10	[42]
	XA	10–500	10	
	HX	10–500	10	
CoFe ₂ O ₄ /rGO	UA	2–10	0.767	The present work
	XA	2–10	0.650	The present work
	HX	2–10	0.506	The present work

Limit of detection (LOD) is calculated using the formula [40]

$$\text{LOD} = \frac{3S}{b}, \quad (10)$$

where S is the standard deviation of the lowest concentration of UA, XN, and HP and b is the slope of calibration curve obtained from the DPV. The detection limits of UA,

XA, and HX obtained in the first range are 0.767, 0.650, and 0.506 μM , respectively. A comparison of the proposed method with other electrochemical approaches for UA, XA, and HX is presented in Table 3. It is notable that the LOD of UA, XA, and HX from the proposed methods is compatible with those based on the modified electrodes reported previously. From the analysis above, we can conclude that CoFe₂O₄/rGO is a potential electrode modifier for determining UA, XA, and HX.

TABLE 4: Determination of UA, XA, and HX in human urine sample.

Samples	Analyte	Detected (mM) Ave \pm SD ($n = 4$)	Added (mM)	Found (mM) Ave \pm SD ($n = 4$)	Rev (%)	Detected by HPLC (mM)
Urine 01	UA	4.31 \pm 0.47	1.50	5.820 \pm 0.270	101.0	4.250
	XA	0.106 \pm 0.004	0.045	0.149 \pm 0.016	95.4	0.111
	HX	<LOD	n/a	n/a	n/a	n/a
Urine 02	UA	1.990 \pm 0.170	1.500	3.440 \pm 0.30	96.4	2.180
	XA	0.059 \pm 0.009	0.045	0.105 \pm 0.015	101.9	0.077
	HX	<LOD	0.750	0.786 \pm 0.042	104.8	n/a
Urine 03	UA	5.57 \pm 0.08	1.500	7.15 \pm 0.75	105.3	5.390
	XA	0.007 \pm 0.001	0.045	0.053 \pm 0.003	101.3	0.012
	HX	<LOD	0.750	0.712 \pm 0.037	95.0	n/a

n/a: not applicable; Ave: average value; SD: standard deviation; n : the number of repetitions of experiments.

3.2.7. Determination of Purine Derivatives in Human Samples. The proposed DPV method was applied to determining the human purine derivatives. The standard addition technique was employed. The recovery experiments were conducted with human urine samples using the CoFe₂O₄/rGO-CGE, and the findings are listed in Table 4. The recoveries found in the range of 95%–105.3% indicate the accuracy and efficiency of the proposed method for the urine samples. The results obtained with HPLC for the real samples are given for comparison. The results from HPLC are comparable with those obtained from the DPV method proposed in this paper (paired sample t -test: $\alpha = 0.05$, $t(5) = 0.5$, $p = 0.637 > 0.05$).

4. Conclusions

In this paper, the CoFe₂O₄/rGO-GCE is fabricated by using a simple method and employed as an electrochemical sensor for the simultaneous detection of UA, XA, and HX with the differential pulse voltammetry technique. The modified electrode has good stability and sensitivity. The results obtained with the proposed method are consistent with those from standard HPLC analysis. Therefore, CoFe₂O₄/rGO is expected to become a potential tool for the assay of UA, XA, and HX both in research and in clinical diagnosis owing to its good precision, high speed, and low cost of analysis.

Data Availability

The data used to support the findings of this study are available from the corresponding author upon request.

Conflicts of Interest

The authors declare that they have no conflicts of interest.

Acknowledgments

The authors are thankful for the financial support from the Vietnamese Ministry of Education and Training for the development of the basic sciences in the fields of chemistry, science of life, science of earth, and science of sea from 2017 to 2025 (Code No. B2019-DQN-562-03).

References

- [1] T. Yamamoto, Y. Moriwaki, and S. Takahashi, "Effect of ethanol on metabolism of purine bases (hypoxanthine, xanthine, and uric acid)," *Clinica Chimica Acta*, vol. 356, no. 1-2, pp. 35–57, 2005.
- [2] E. Caussé, A. Pradelles, B. Dirat, A. Negre-Salvayre, R. Salvayre, and F. Couderc, "Simultaneous determination of allantoin, hypoxanthine, xanthine, and uric acid in serum/plasma by CE," *Electrophoresis*, vol. 28, no. 3, pp. 381–387, 2007.
- [3] J. R. Klinenberg, S. Goldfinger, K. H. Bradley, and J. E. Seegmiller, "An enzymatic spectrophotometric method for the determination of xanthine and hypoxanthine," *Clinical Chemistry*, vol. 13, no. 10, pp. 834–846, 1967.
- [4] R. Boulieu, C. Bory, P. Baltassat, and C. Gonnet, "High-performance liquid chromatographic determination of hypoxanthine and xanthine in biological fluids," *Journal of Chromatography B: Biomedical Sciences and Applications*, vol. 233, no. 1, pp. 131–140, 1982.
- [5] N. Cooper, R. Khosravan, C. Erdmann, J. Fiene, and J. W. Lee, "Quantification of uric acid, xanthine and hypoxanthine in human serum by HPLC for pharmacodynamic studies," *Journal of Chromatography B*, vol. 837, no. 1-2, pp. 1–10, 2006.
- [6] J.-M. Zen, Y.-Y. Lai, H.-H. Yang, and A. S. Kumar, "Multianalyte sensor for the simultaneous determination of hypoxanthine, xanthine and uric acid based on a preanodized nontronite-coated screen-printed electrode," *Sensors and Actuators B: Chemical*, vol. 84, no. 2-3, pp. 237–244, 2002.
- [7] A. S. Kumar and P. Swetha, "Ru(DMSO)₄Cl₂ nano-aggregated Nafion membrane modified electrode for simultaneous electrochemical detection of hypoxanthine, xanthine and uric acid," *Journal of Electroanalytical Chemistry*, vol. 642, no. 2, pp. 135–142, 2010.
- [8] Y. Wang and L.-l. Tong, "Electrochemical sensor for simultaneous determination of uric acid, xanthine and hypoxanthine based on poly (bromocresol purple) modified glassy carbon electrode," *Sensors and Actuators B: Chemical*, vol. 150, no. 1, pp. 43–49, 2010.
- [9] F. Zhang, Z. Wang, Y. Zhang et al., "Simultaneous electrochemical determination of uric acid, xanthine and hypoxanthine based on poly(l-arginine)/graphene composite film modified electrode," *Talanta*, vol. 93, pp. 320–325, 2012.

- [10] G. El-Shobaky, A. Turkey, N. Mostafa, and S. Mohamed, "Effect of preparation conditions on physicochemical, surface and catalytic properties of cobalt ferrite prepared by coprecipitation," *Journal of Alloys and Compounds*, vol. 493, no. 1-2, pp. 415-422, 2010.
- [11] I. Sandu, L. Presmanes, P. Alphonse, and P. Tailhades, "Nanostructured cobalt manganese ferrite thin films for gas sensor application," *Thin Solid Films*, vol. 495, no. 1-2, pp. 130-133, 2006.
- [12] V. A. Kumary, J. Divya, T. M. Nancy, and K. Sreevalsan, "Voltammetric detection of paracetamol at cobalt ferrite nanoparticles modified glassy carbon electrode," *International Journal of Electrochemical Science*, vol. 8, pp. 6610-6619, 2013.
- [13] J.-T. Han, K.-J. Huang, J. Li, Y.-M. Liu, and M. Yu, " β -Cyclodextrin-cobalt ferrite nanocomposite as enhanced sensing platform for catechol determination," *Colloids and Surfaces B: Biointerfaces*, vol. 98, pp. 58-62, 2012.
- [14] F. S. Yardımcı, M. Şenel, and A. Baykal, "Amperometric hydrogen peroxide biosensor based on cobalt ferrite-chitosan nanocomposite," *Materials Science and Engineering: C*, vol. 32, no. 2, pp. 269-275, 2012.
- [15] A. A. Ensafi, H. A. Alinajafi, M. Jafari-Asl, B. Rezaei, and F. Ghazaei, "Cobalt ferrite nanoparticles decorated on exfoliated graphene oxide, application for amperometric determination of NADH and H_2O_2 ," *Materials Science and Engineering: C*, vol. 60, pp. 276-284, 2016.
- [16] Z.-S. Wu, W. Ren, L. Gao et al., "Synthesis of graphene sheets with high electrical conductivity and good thermal stability by hydrogen arc discharge exfoliation," *ACS Nano*, vol. 3, no. 2, pp. 411-417, 2009.
- [17] S. Pei and H.-M. Cheng, "The reduction of graphene oxide," *Carbon*, vol. 50, no. 9, pp. 3210-3228, 2012.
- [18] Z.-H. Sheng, X.-Q. Zheng, J.-Y. Xu, W.-J. Bao, F.-B. Wang, and X.-H. Xia, "Electrochemical sensor based on nitrogen doped graphene: simultaneous determination of ascorbic acid, dopamine and uric acid," *Biosensors and Bioelectronics*, vol. 34, no. 1, pp. 125-131, 2012.
- [19] M. A. Raj and S. A. John, "Simultaneous determination of uric acid, xanthine, hypoxanthine and caffeine in human blood serum and urine samples using electrochemically reduced graphene oxide modified electrode," *Analytica Chimica Acta*, vol. 771, pp. 14-20, 2013.
- [20] Y. Wei, C. Gao, F.-L. Meng et al., " SnO_2 /reduced graphene oxide nanocomposite for the simultaneous electrochemical detection of cadmium (II), lead (II), copper (II), and mercury (II): an interesting favorable mutual interference," *The Journal of Physical Chemistry C*, vol. 116, pp. 1034-1041, 2011.
- [21] J. Li, D. Kuang, Y. Feng, F. Zhang, Z. Xu, and M. Liu, "A graphene oxide-based electrochemical sensor for sensitive determination of 4-nitrophenol," *Journal of Hazardous Materials*, vol. 201, pp. 250-259, 2012.
- [22] W. S. Hummers Jr. and R. E. Offeman, "Preparation of graphitic oxide," *Journal of the American Chemical Society*, vol. 80, no. 6, pp. 1339-1339, 1958.
- [23] T. Qi, C. Huang, S. Yan, X.-J. Li, and S.-Y. Pan, "Synthesis, characterization and adsorption properties of magnetite/reduced graphene oxide nanocomposites," *Talanta*, vol. 144, pp. 1116-1124, 2015.
- [24] R. Waldron, "Infrared spectra of ferrites," *Physical review*, vol. 99, no. 6, pp. 1727-1735, 1955.
- [25] M. Zhang and M. Jia, "High rate capability and long cycle stability Fe_3O_4 -graphene nanocomposite as anode material for lithium ion batteries," *Journal of Alloys and Compounds*, vol. 551, pp. 53-60, 2013.
- [26] D. Barreca, C. Massignan, S. Daolio et al., "Composition and microstructure of cobalt oxide thin films obtained from a novel cobalt (II) precursor by chemical vapor deposition," *Chemistry of Materials*, vol. 13, no. 2, pp. 588-593, 2001.
- [27] D. G. Castner, P. R. Watson, and I. Y. Chan, "X-ray absorption spectroscopy, X-ray photoelectron spectroscopy, and analytical electron microscopy studies of cobalt catalysts. 2. Hydrogen reduction properties," *Journal of Physical Chemistry*, vol. 94, no. 2, pp. 819-828, 1990.
- [28] T. Jafari, E. Moharreri, A. S. Amin, R. Miao, W. Song, and S. L. Suib, "Photocatalytic water splitting—the untamed dream: a review of recent advances," *Molecules*, vol. 21, no. 7, p. 900, 2016.
- [29] X. Zeng, L. Zhu, G. Jiang, C. Wang, Z. Xia, and R. Yu, "Template-free formation of uniform Fe_3O_4 hollow nanoflowers supported on reduced graphene oxide and their excellent microwave absorption performances," *Physica Status Solidi (a)*, vol. 215, no. 7, article 1701049, 2018.
- [30] B. Qu, C. Zhu, C. Li, X. Zhang, and Y. Chen, "Coupling hollow Fe_3O_4 -Fe nanoparticles with graphene sheets for high-performance electromagnetic wave absorbing material," *ACS Applied Materials & Interfaces*, vol. 8, pp. 3730-3735, 2015.
- [31] P. Peerakiatkhaohn, J. H. Yun, H. Chen, M. Lyu, T. Butburee, and L. Wang, "Stable hematite nanosheet photoanodes for enhanced photoelectrochemical water splitting," *Advanced Materials*, vol. 28, no. 30, pp. 6405-6410, 2016.
- [32] T. Zhu, S. Chang, Y.-F. Song, M. Lahoubi, and W. Wang, "PVP-encapsulated $CoFe_2O_4$ /rGO composites with controllable electromagnetic wave absorption performance," *Chemical Engineering Journal*, vol. 373, pp. 755-766, 2019.
- [33] K. Zhang, J. Li, F. Wu, M. Sun, Y. Xia, and A. Xie, "Sandwich $CoFe_2O_4$ /RGO/ $CoFe_2O_4$ nanostructures for high-performance electromagnetic absorption," *ACS Applied Nano Materials*, vol. 2, pp. 315-324, 2018.
- [34] Y. Yao, Z. Yang, D. Zhang, W. Peng, H. Sun, and S. Wang, "Magnetic $CoFe_2O_4$ -graphene hybrids: facile synthesis, characterization, and catalytic properties," *Industrial & Engineering Chemistry Research*, vol. 51, no. 17, pp. 6044-6051, 2012.
- [35] J. Soleymani, M. Hasanzadeh, N. Shadjou et al., "A new kinetic-mechanistic approach to elucidate electrooxidation of doxorubicin hydrochloride in unprocessed human fluids using magnetic graphene based nanocomposite modified glassy carbon electrode," *Materials Science and Engineering: C*, vol. 61, pp. 638-650, 2016.
- [36] A. J. Bard and L. R. Faulkner, "Fundamentals and applications," *Electrochemical Methods*, vol. 2, pp. 580-632, 2001.
- [37] E. Laviron, "General expression of the linear potential sweep voltammogram in the case of diffusionless electrochemical systems," *Journal of Electroanalytical Chemistry and Interfacial Electrochemistry*, vol. 101, no. 1, pp. 19-28, 1979.
- [38] D. Kang, "On the elliptic problems with critical weighted Sobolev-Hardy exponents," *Nonlinear Analysis: Theory, Methods & Applications*, vol. 66, no. 5, pp. 1037-1050, 2007.
- [39] W. Horwitz and R. Albert, "Quality Issues The concept of uncertainty as applied to chemical measurements," *Analyst*, vol. 122, no. 6, pp. 615-617, 1997.

- [40] S. K. Ponnaiah, P. Periakaruppan, and B. Vellaichamy, "New electrochemical sensor based on a silver-doped iron oxide nanocomposite coupled with polyaniline and its sensing application for picomolar-level detection of uric acid in human blood and urine samples," *The Journal of Physical Chemistry B*, vol. 122, no. 12, pp. 3037–3046, 2018.
- [41] F. Pan, T.-M. Chen, J.-J. Cao, J.-P. Zou, and W. Zhang, "Ga(ClO₄)₃-catalyzed synthesis of quinoxalines by cycloaddition of α -hydroxyketones and *o*-phenylenediamines," *Tetrahedron Letters*, vol. 53, no. 20, pp. 2508–2510, 2012.
- [42] R. Goyal, A. Mittal, and S. Sharma, "Simultaneous voltammetric determination of hypoxanthine, xanthine, and uric acid," *Electroanalysis*, vol. 6, no. 7, pp. 609–611, 1994.